AIAA JOURNAL
Vol. 43, No. 11, November 2005

Large-Eddy Simulation of Transitional Boundary Layer with Impinging Shock Wave

Susumu Teramoto*
University of Tokyo, Tokyo 113-8656, Japan

The transition of a boundary layer on a flat plate with an impinging shock wave is studied numerically by compressible large-eddy simulation using a hybrid compact/Roe scheme. The numerical code is verified by comparison with experimental observations of shock wave/turbulent boundary-layer interaction and then applied for the analysis of shock wave/transitional boundary-layer interaction. The simulation provides accurate results with respect to the location of reattachment and the boundary-layer properties downstream of reattachment. Large-scale coherent structures such as longitudinal vortex pairs, low-speed streaks, and hairpin vortices are identified in the transitional region, and it is revealed that these coherent structures play important roles in the transition. Thus, it is important to resolve these structures adequately to obtain an accurate prediction of the reattachment point. The subsequent breakdown of these coherent structures have smaller length scales, and resolving the breakdown requires much finer grid resolution. However, the influence of underresolution of breakdown on the downstream flowfield can be largely ignored under the conditions examined. Large-eddy simulation is, therefore, useful for the qualitative analysis of flowfields involving a supersonic transitional boundary layer.

Nomenclature

C_f	=	time-mean skin-friction coefficient
f_θ	=	shock sensor function
Lx, Ly, Lz	=	extent of the computational domain
Nx, Ny, Nz	=	number of grid points
p	=	static pressure
Q	=	second invariant of velocity gradient tensor
Re	=	Reynolds number
Tu	=	turbulent intensity
$\bar{U}$	=	time- and spanwise-averaged streamwise velocity
u, v, w	=	Cartesian velocity components in x, y, and z directions
u_τ	=	friction velocity
x, y, z	=	Cartesian coordinate in the streamwise, vertical, and spanwise directions
Δt	=	time step size
$\Delta x, \Delta y, \Delta z$	=	mesh step size
δ	=	boundary-layer thickness
δ_1	=	boundary-layer displacement thickness
μ	=	viscosity
ν	=	dynamic viscosity
ρ	=	density
ω	=	vorticity

Subscripts

rms	=	root mean square
w	=	evaluated at wall
∞	=	evaluated at freestream

Superscripts

~	=	Favre-averaged value
-	=	time-averaged value
^	=	test-filtered value
$'$	=	fluctuating component
$+$	=	value given in wall unit

Received 16 February 2005; revision received 11 July 2005; accepted for publication 12 July 2005.

*Lecturer, Department of Aeronautics and Astronautics, Hongo 7-3-1, Bunkyo-ku; teramoto@thermo.t.u-tokyo.ac.jp. Member AIAA.

Introduction

THE flowfield in turbomachinery is bounded by solid walls. Because the Reynolds number of the flow is relatively low, the development of a boundary layer has a significant impact on the stability and performance of turbomachinery cascade flows. Prediction of the development of such a boundary layer is a key issue in the design and analysis of cascades. However, the boundary layer inside modern gas turbines, where the tip speed can reach 450–500 m/s, interacts with shock waves in a transonic flowfield and, thus, is far more complicated than in external flows. The chord Reynolds number of a typical gas turbine ranges from 10^5 to 10^6 (Ref. 1), but at high altitude or in very small gas turbines, this value may be one or two orders of magnitude lower, at which the effect of the boundary-layer transition is not negligible.

Because it is almost impossible to take account of all of these effects in the analysis of cascade flows, a Reynolds-averaged Navier–Stokes (RANS) equation coupled with a turbulence model originally developed for the analysis of a steady attached boundary layer is often used for numerical simulation. When the Reynolds number is not sufficiently high to allow fully turbulent flow to be assumed, an empirical transition model is combined with the turbulence model.[2–4] This approach provides satisfactory results if the model parameters have been determined appropriately. However, because parameter tuning always requires experimental data, the application of this technique to a flowfield for which similar experimental data are not available is questionable. Shock wave/transitional boundary-layer interaction is a typical flowfield for which it is difficult to find appropriate parameters. Hilgenfeld et al.[4] performed a numerical study of linear cascade flow at $Re_c = 4.5 \times 10^5$ using Spalart-Allmaras's turbulence model and the Abu-Ghannam/Shaw transition model. Hilgenfeld et al.[4] reported that their numerical results were in good agreement with experimental measurements for weak shock waves, but tended to underestimate the loss coefficient at high transonic regimes, at which both turbulent transition and severe shock wave/boundary layer interaction (SWBLI) take place. To extend the applications of gas turbines to situations of low Reynolds number, such as at high altitude or in small devices, it is important to improve the reliability of numerical simulation of such flowfields.

Clearly, direct numerical simulation (DNS) or large-eddy simulation (LES) is an attractive choice for this type of analysis. DNS/LES

has recently been applied for the analysis of SWBLI.[5,6] Knight et al.[7] reviewed recent numerical simulations of SWBLI and concluded that DNS/LES provides very good results for two-dimensional and low-Reynolds-number SWBLI. DNS/LES has also been applied successfully to the transition of low-speed boundary layers including natural transitions,[8,9] transitions in laminar separation bubbles,[10,11] and bypass transitions.[12,13] Abdulmalik et al.[14] also reported an analysis of shock/transitional boundary layer interaction by DNS but focused mainly on a two-dimensional views of turbulent statistics, with no effort made to compare the numerical results with experiments.

Inasmuch as it remains very difficult to apply DNS for the analysis of flowfields at Reynolds numbers of the order of 10^5, LES is used in practical applications. However, it is unclear whether simulation of the entire transition process can be achieved within the framework of LES because simulation of streak breakdown on the path to turbulence requires very fine spatial resolution,[12] and it is questionable whether subgrid-scale models developed assuming an energy cascade function properly in the transitional flowfield. Nevertheless, from an engineering point of view, more accurate predictions of key parameters, such as the locations of reattachment and boundary-layer thickness after reattachment, than those provided by RANS will be of major benefit in numerical simulations.

The objective of present report is to apply LES for the analysis of shock wave/transitional boundary-layer interaction and study the influence of computational parameters on the results, as well as to investigate the reliability of LES when applied to the analysis of such a flowfield.

Numerical Method

Governing Equations and Discretization

Spatially filtered three-dimensional Navier–Stokes equations are employed for numerical simulations following the formulation presented by Vreman[15] and Garnier et al.[5] The first spatial derivative terms appearing in the governing equations are evaluated by using the sixth-order accurate compact difference scheme.[16] Numerical instability is suppressed by filtering the conservative properties using a 10th-order implicit spatial filter[17] once every time step. Because the use of compact differences near discontinuities leads to nonphysical oscillation, spatial derivatives in the convective terms are evaluated using the Roe scheme extended to higher orders by MUSCL interpolation with minmod limiter in the regions near shock waves (see Ref. 6). The 10th-order implicit spatial filter is also turned off at the region where the high-order method is degraded to the Roe scheme. The classical Jameson-type shock sensor multiplied by the Ducros et al. sensor function,[18] that is,

$$\left|\frac{\bar{p}_{j+1}-2\bar{p}_j+\bar{p}_{j-1}}{\bar{p}_{j+1}+2\bar{p}_j+\bar{p}_{j-1}}\right|\frac{(\operatorname{div}\tilde{u})^2}{(\operatorname{div}\tilde{u})^2+(\operatorname{rot}\tilde{u})^2+\varepsilon}$$

is used for the detection of shock waves. The viscous terms are evaluated by successive application of a first-derivative operator. The stress tensor is first evaluated at each node using the fourth-order central difference, and the derivative of the stress tensor is evaluated by the same fourth-order central difference scheme to form the viscous flux.

Subgrid scale (SGS) terms are evaluated by using the selective mixed-scale model[19]:

$$\nu_t = f_\theta C_m \sqrt{|S|}\left(q_c^2\right)^{\frac{1}{4}}\Delta^{\frac{3}{2}}$$

Here, S is the resolved stress tensor and q_c^2 is the test field kinetic energy, which is evaluated by $q_c^2=\frac{1}{2}(\tilde{u}_i-\hat{\tilde{u}}_i)^2$, where the caret denotes the test filter. The selective function f_θ is defined as

$$f_\theta=\begin{cases}1, & \text{if} \quad \theta\geq\theta_0\\ \left(\dfrac{\tan^2(\theta/2)}{\tan^2(\theta_0/2)}\right)^2, & \text{otherwise}\end{cases}$$

where θ is the angle between the local vorticity ω and the test-filtered vorticity $\hat{\omega}$. This model is simple and does not require an ad hoc damping function near the wall because the SGS viscosity automatically becomes zero in the laminar region.

The second-order accurate implicit Crank–Nicolson scheme is used for time integration, and the fourth-order accurate compact scheme (see Ref. 20) is also applied for evaluation of the spatial derivative term on the left-hand side. Errors caused by linearization and diagonalization are eliminated by Newton subiteration. In the present study, three subiterations were sufficient to achieve a two-order reduction of the residual at a Courant–Friedrichs–Lewy (CFL) number of 2.

Boundary Conditions

The lower boundary is defined as a nonslip adiabatic wall, and the spanwise boundaries are set as periodic boundaries. Thompson's nonreflective boundary condition[21] is applied for the upper and outlet boundaries, and a sponge layer[22] is introduced at the outlet boundary to attenuate turbulent fluctuations.

At the inlet boundary above the incident shock wave, all physical properties are simply fixed at those behind the oblique shock wave. Mean physical properties below the incident shock wave are fixed at the profiles obtained from two-dimensional laminar computation, and a freestream turbulent fluctuation is superimposed over the mean profile.

Isotropic decaying turbulence is used to generate the inflow turbulence. The simulation of the decaying turbulence is started from a divergence-free velocity field under uniform density and pressure and is continued until the desired turbulence intensity is achieved, at which point the turbulent flowfield is frozen in time. The time-varying fluctuation is obtained from the frozen turbulence by sampling the physical properties over a plane that sweeps the frozen turbulence at the freestream velocity.

Verification

The reliability of this new code is verified through comparison with published data. Garnier et al.[5] reported an LES for shock wave/turbulent boundary-layer interaction and compared the numerical results with experimental data. The present code is applied to the same flowfield for direct comparison. The geometry of the computational domain is shown in Fig. 1. The freestream Mach number is 2.3, the Reynolds number based on the displacement thickness at the inlet boundary and the freestream properties is 1.9132×10^4, and the deflection angle of the incident shock wave is 8 deg. The number of grid points, $255\times151\times55$, is the same as that of grid A presented in the report of Garnier et al. Although the definition of edge velocity that will be used for the evaluation of friction coefficient is somewhat arbitrary, it is defined here as the velocity at which w_{rms} falls below 1% of its maximum value.

Figure 2 shows a comparison of the results of the present simulation with the results of Garnier et al. The simulated friction coefficient is in satisfactory agreement with the experimental result. The extent of separation in the present simulation ($x=303$–332 mm) is closely consistent with that observed in the experiment[5] ($x=300$–332 mm). The displacement thickness of the incoming boundary layer δ_1 is 3.5 mm in the experiment and 3.2 mm

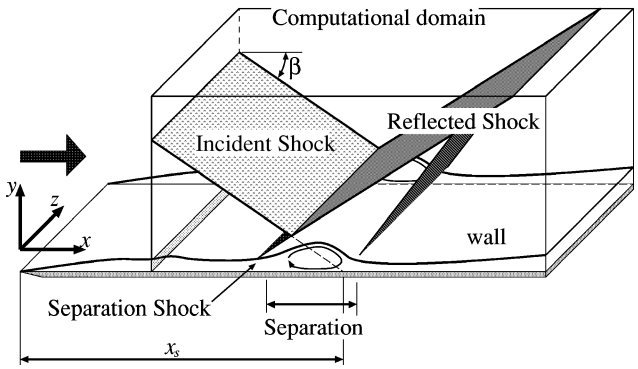

Fig. 1 Shock wave/boundary-layer interaction.

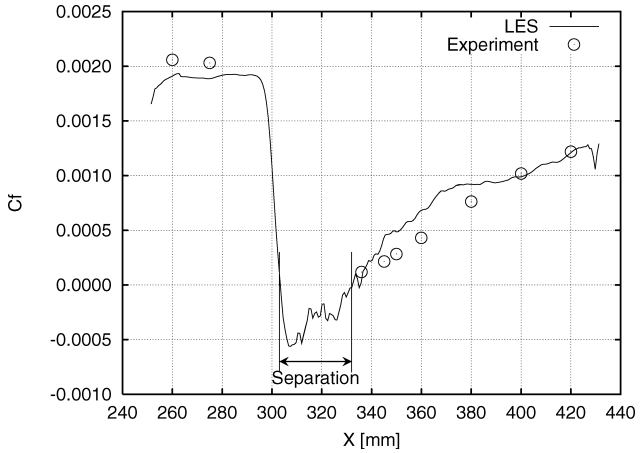

a) Local friction coefficient

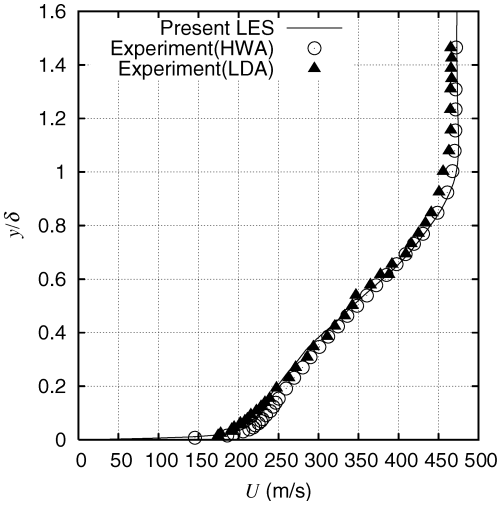

b) Mean velocity profile after reattachment, $x = 420$ mm

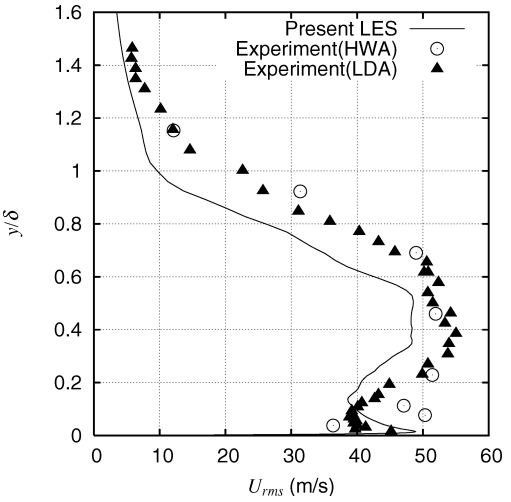

c) Longitudinal fluctuation velocity profile after reattachment, $x = 420$ mm

Fig. 2 Shock/turbulent boundary-layer interaction.

in the present LES, so that the separation size is approximately 8–9 times of δ_1. The velocity profile downstream of the reattachment is coincident with the experimental data, and the fluctuation velocity is also reproduced qualitatively. Other plots (not shown) also exhibit a trend similar to those reported by Garnier et al., demonstrating that the accuracy of the present code is generally comparable to that of Garnier et al.

Flow Condition and Computational Grids

The geometry of the flowfield studied here is the same as that shown in Fig. 1, although the incoming boundary layer in this case is defined as being laminar. Hakkinen et al.[23] carried out wind-tunnel experiments on shock wave/laminar boundary-layer interaction and obtained measurements of the pitot pressure profile inside the boundary layer, which on conversion afforded velocity and friction coefficients. The flow conditions in the present numerical simulation correspond to those in Hakkinen's experiments, where the measured friction coefficient corresponds to the conditions of turbulent reattachment.

Note that the evaluation of the experimental friction coefficient involves some uncertainty. The friction coefficient in the Hakkinen et al.[23] experiments was determined from the reading of the pitot tube at rest on the wall. However, because the correlation between the pitot pressure and the friction coefficient was calibrated only for the attached boundary layer without pressure gradient, there remains uncertainty for the region in which the boundary layer is not in equilibrium. Therefore, the experimental-friction coefficient will be used only for qualitative discussion in this study, such as evaluation of the locations of separation and reattachment or the distinction between laminar and turbulent boundary layers.

The freestream Mach number in the present simulation is set at 2.0, the shock pressure ratio is set at 1.91, and the Reynolds number based on the distance between the leading edge and the shock incident point is defined as 3.29×10^5. Hakkinen defined the pressure ratio as that between the pressure behind the reflected shock wave and that upstream of the incident shock wave. In the present study, the pressure ratio across the incident shock wave is approximately 1.39, and the incident shock angle β is 35.36 deg.

Because no information is provided regarding the turbulence characteristics of the wind tunnel used in the Hakkinen et al.[23] experiment, the numerical results were obtained for four different turbulence levels in this study, $Tu = 1.2$, 0.6, 0.06, and 0% (no imposed freestream turbulence). It was confirmed that the transition occurred even at the lowest turbulence level. The separation and reattachment points both move depending on the inlet turbulence, but the structure of the flowfield was found to remain essentially the same. Therefore, the results for $Tu = 0.6\%$, which showed the best agreement with the experiments, are used in the following discussion.

The number of grid points and the grid resolutions are listed in Table 1, where the grid resolutions are given in wall units $\{x^+ = (\rho_w u_\tau/\mu_w)x$ and $u_\tau = \sqrt{[\mu_w(\partial u/\partial y)/\rho_w]}\}$ at two locations: $x = 75$ mm, where the friction coefficient reaches a maximum, and $x = 95$ mm, where the boundary layer reaches an equilibrium state and the velocity profile follows a log-law curve.

Table 1 Computational grids[a]

Grid	L_x	L_y	L_z	N_x	N_y	N_z	Δx^+		$\Delta y^+_{\min}$		Δz^+	
							$x=75$	$x=95$	$x=75$	$x=95$	$x=75$	$x=95$
A	105.0	60.0	5.12	601	121	99	16.6	33.4	0.86	0.73	11.4	9.7
B	105.0	60.0	5.12	401	121	65	41.8	37.2	0.84	0.74	16.7	14.9
C	105.0	60.0	5.12	301	121	44	60.2	54.4	0.80	0.73	24.3	22.0
D	105.0	60.0	5.12	201	121	33	81.4	70.2	0.81	0.70	32.5	28.1
E	164.4	60.0	5.12	698	121	65	41.9	37.1	0.84	0.74	16.8	14.9

[a]Length in millimeters.

Table 2 Spanwise extent of computational domain

Method	Transition type	Based on inlet properties		Based on downstream properties L_z^+
		δ_{in}	$\delta_{1\text{in}}$	
Present LES	Separated	$10\delta_{\text{in}}$	$25\delta_{1\text{in}}$	950
Yang and Voke[11]	Separated	——	——	570
Alam and Sandham[10]	Separated	——	$30\delta_{1\text{in}}$	——
Jacobs and Durbin[12]	Bypass	$30\delta_{\text{in}}$	——	——
Berlin et al.[9]	Oblique	——	$60\delta_{1\text{in}}$	——

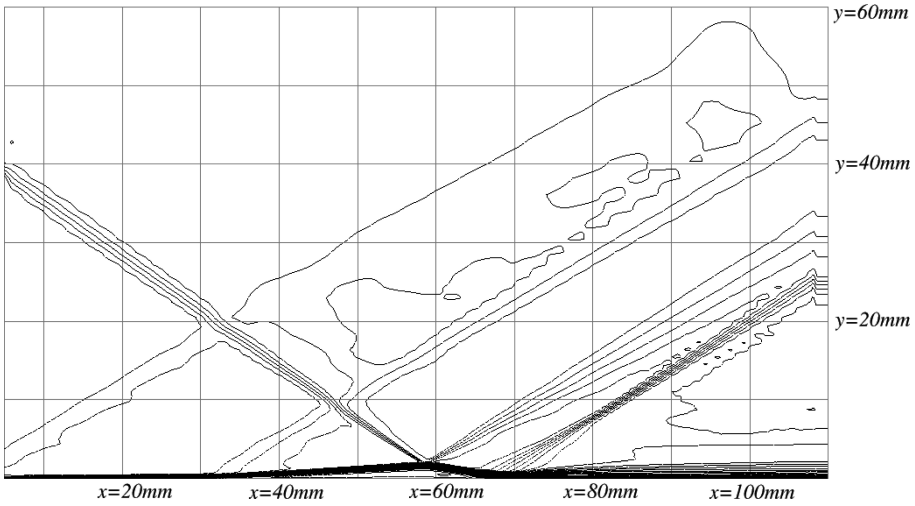

Fig. 3 Mean Mach number contours.

The computational domains for grids A–D are all of the same size. Thus, the influence of grid resolution is investigated using these grids. The resolution of grid A is comparable with that used in the LES of the separated boundary-layer transition[11] ($\Delta x^+ = 10 \sim 30.5$ and $\Delta z^+ = 9$), and the resolution of grid C is the same as that used in the LES of the transition in the attachment-line boundary layer[24] ($\Delta x^+ = 56$ and $\Delta z^+ = 39$). In grid E, which is defined with the same grid resolution as grid B, the outlet boundary is located farther downstream to provide data on the influence of the outlet boundary.

The boundary-layer thickness near the outlet ($x = 95$ mm) $\delta_{x=95}$ is approximately 1.9 mm. Therefore, the size of the computational domain except grid E is

$$L_x/\delta_{x=95} = 55, \qquad L_y/\delta_{x=95} = 32, \qquad L_z/\delta_{x=95} = 2.7$$

L_x and L_y were determined from the geometry of the Hakkinen et al. experiment,[23] and $L_z/\delta_{x=95}$ was taken to be similar to that of Rizzetta et al.[6] ($L_z = 2.9\delta_0$). Note that initial stage of boundary-layer transition is characterized by disturbance with large length scale, and so LES/DNS of transition generally requires a computational domain with wider spanwise extent. Table 2 compares spanwise extent of the present computational domain with those of other studies. The extent of the present computational domain is comparable to those of other simulations of separated flow transition.

The time step Δt was approximately 2.2×10^{-8} s so that the maximum CFL number was less than 2.

Results

Time-Averaged Flowfield

Figure 3 shows the contours of the mean Mach number. The incoming laminar boundary layer interacts with the oblique shock wave at $x = 58$ mm, and the boundary layer separates substantially upstream of this point ($x = 30$ mm), although the compression wave generated at the separation point is very weak. The separated boundary layer reattaches at around $x = 70$ mm to form a reattachment shock wave. The boundary layer downstream of the reattachment is considerably thicker than the incoming boundary layer, indicating a turbulent transition. The Reynolds stress distribution in Fig. 4 shows that the Reynolds stress develops inside the separated shear layer, taking a maximum just upstream of the reattachment point and gradually diminishing downstream.

Instantaneous distribution of the shock sensor function in Fig. 5 shows that the shock sensor function used in the present study successfully distinguished shock waves from turbulent pressure fluctuation and the turbulent boundary layer is mostly resolved by the high-order compact scheme.

Figure 6 shows the mean streamwise velocity profile downstream of the reattachment point. The velocity is plotted using the van Driest

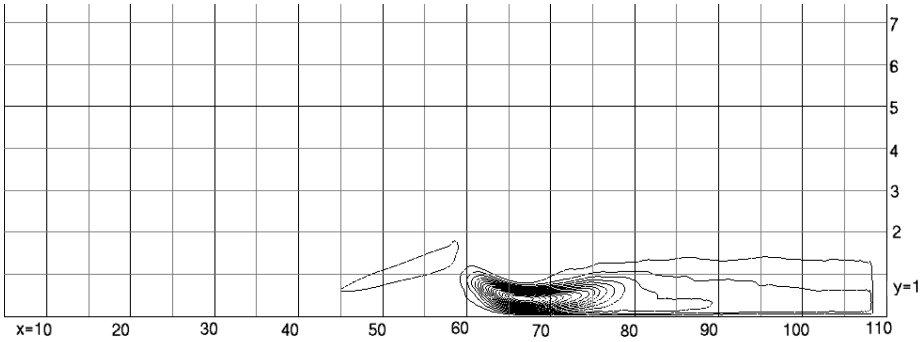

Fig. 4 Reynolds stress distribution, $y \times 5$.

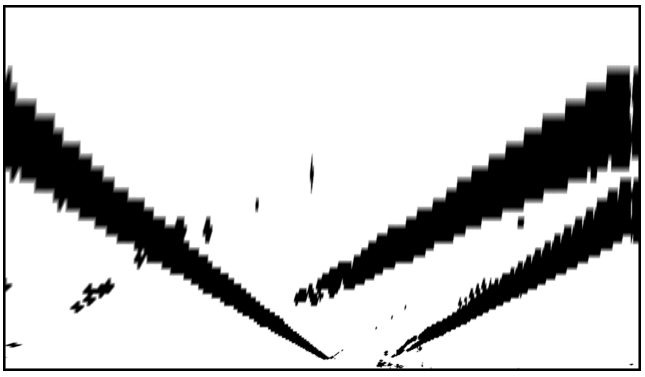

Fig. 5 Instantaneous distributon of shock sensor function.

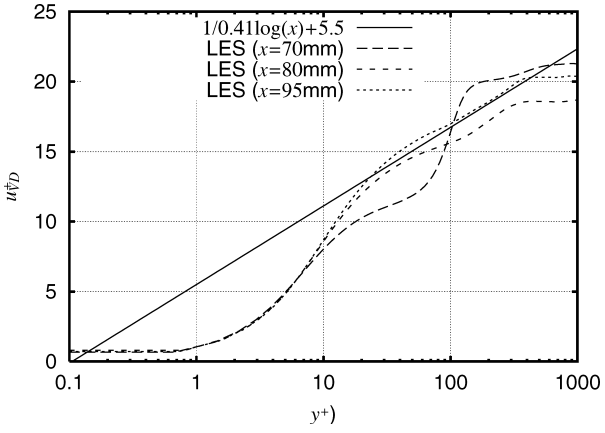

Fig. 6 Mean longitudinal velocity profiles.

transformation[25] u^+_{VD} to account for the density variation, as given by

$$u^+_{VD} = \int^{u^+} \sqrt{\frac{\rho}{\rho_w}}\, \mathrm{d}[u^+(y)], \qquad u^+ = \frac{u}{u_\tau}$$

The velocity distribution gradually approaches a turbulent profile and converges to law of the wall at $x = 95$ mm. Velocity fluctuations u_{rms}, v_{rms}, and w_{rms} at $x = 95$ mm are compared with DNS by Spalart[26] (incompressible, $Re_\theta = 1.410 \times 10^3$) in Fig. 7. Profiles near the wall ($y^+ < 20$) agree with DNS of the equilibrium turbulent boundary layer, but u_{rms} at the outer part falls below Spalart's DNS. Figures 6 and 7 show that the boundary layer downstream of the reattachment is turbulent while it is not in complete equilibrium.

The velocity profiles and local friction coefficient are compared with the results of the Hakkinen et al.[23] experiment in Figs. 8 and 9. Here, the friction coefficient C_f is defined as

$$C_f = \frac{\mu_w(\partial \bar{u}/\partial y)|_w}{\frac{1}{2}\rho_\infty u_\infty^2}$$

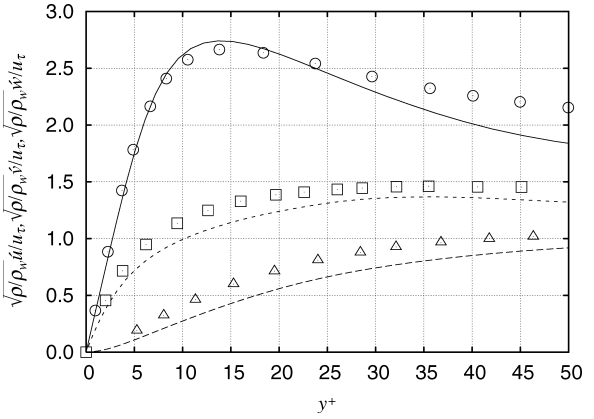

Fig. 7 Velocity fluctuation profiles at $x = 95$ mm: ——, present LES u_{rms}; – – –, present LES v_{rms}; . . . , present LES w_{rms}; ○, DNS by Spalart u_{rms}; △, DNS by Spalart v_{rms}; and □, DNS by Spalart w_{rms}.

where subscripts ∞ and w denote the freestream properties upstream of the incident shock wave and the properties at the wall.

The predicted velocity profiles agree very well with the experimental data, except in the regions of strong shock interaction. The agreement of the locations of separation and reattachment are also satisfactory, although the simulated separation region is slightly wider than that observed in the experiment. The rapid increase in the friction coefficient at $x = 70$ mm indicates that the boundary layer reattaches as a turbulent boundary layer. Although the friction coefficients overshoot the experimental value in the reattachment region, Fig. 8e shows that the simulated velocity profile is still closely consistent with the experimental results in this region, indicating that the discrepancy in the friction coefficient is likely to be due to uncertainties in the conversion from pitot pressure to friction coefficient.

The friction coefficients downstream of the reattachment show that the coarsest grid (grid D) underpredicts the friction coefficient of the attached turbulent boundary layer, whereas the other finer grids produce consistent curves. On close inspection of the friction coefficients near the point of reattachment, it becomes clear that grid C, which resolved the attached turbulent boundary layer well, predicts the reattachment point to be slightly downstream of that indicated in the other three finer grids. The reattachment points for grids B and E coincide with that for grid A. Thus, the influence of refinement only appears in the maximum value of the friction coefficient. Furthermore, because the results for grids B and E follow the same curve, the position of the exit boundary appears to have no influence on the distribution of the friction coefficient.

Movement of the separation point can also be observed in addition to movement of the reattachment point. The wall pressure distribution (Fig. 10) reveals that when the shear layer reattaches upstream, the expansion behind the incident shock wave becomes stronger, lowering the pressure in the separation region and inducing separation downstream. Although the difference in pressure in the separation region is less than 1% of the freestream static pressure,

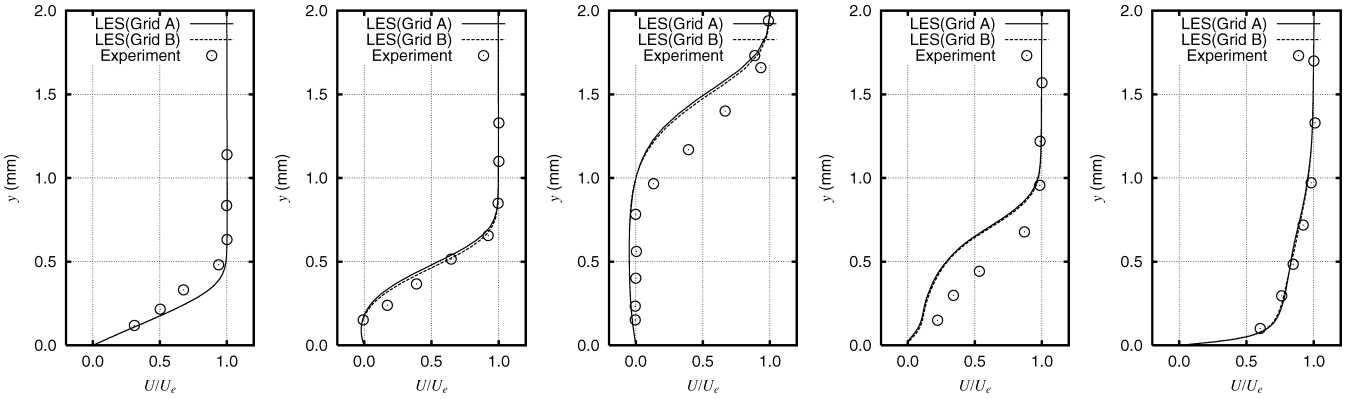

a) $x = 27.9$ mm b) $x = 38.1$ mm c) $x = 55.9$ mm d) $x = 66.0$ mm e) $x = 73.7$ mm

Fig. 8 Mean longitudinal velocity profiles near the separation bubble, grids A and B.

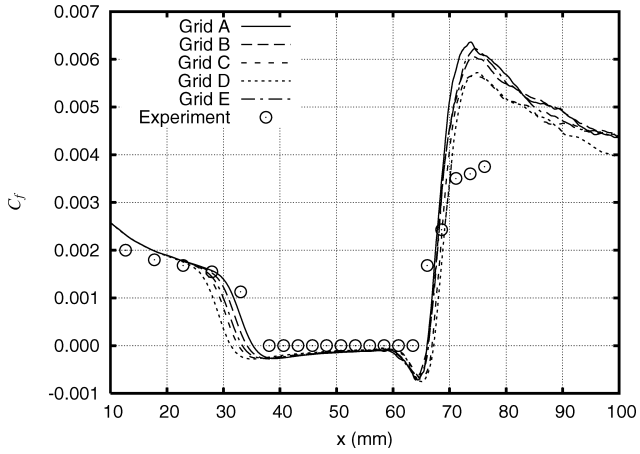

a) Entire region

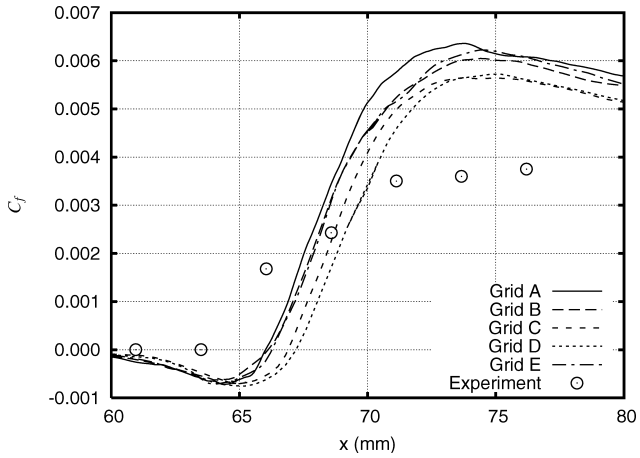

b) Near reattachment point

Fig. 9 Local skin-friction coefficient.

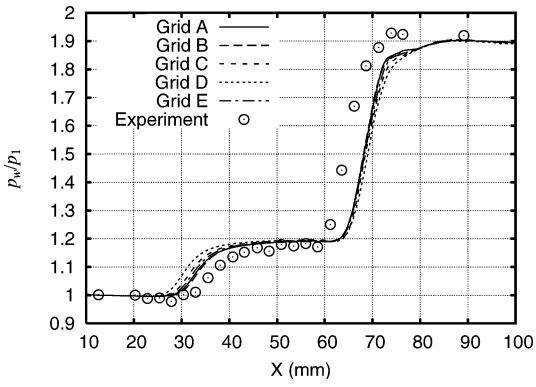

a) Entire region

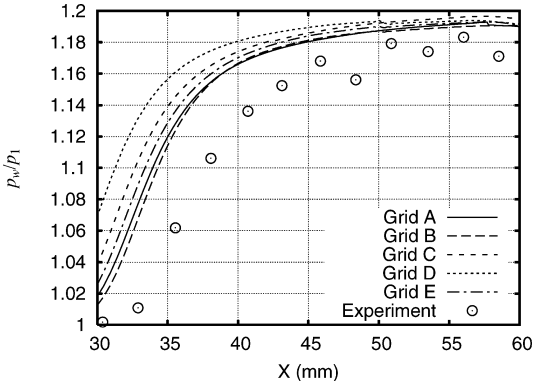

b) Near separation point

Fig. 10 Wall pressure distribution.

the separation point is quite sensitive to the pressure in the separation region because the boundary-layer upstream of the separation is laminar. Therefore, the shift of the separation point is not due directly to the grid resolution, but rather represents a secondary effect induced by the movement of the reattachment point.

Figure 11 shows the profiles of wall-normal fluctuation velocity v_{rms}. These profiles clearly show the dependence of v_{rms} in the reattachment region on the grid resolution. That is, a finer grid results in a larger value of v_{rms} and grid convergence is not achieved within the grid resolutions studied here. In particular, the discrepancy of v_{rms} for the coarsest (grid D) at the edge of the boundary layer ($y \sim 3.0$ mm) is noticeable. The evolution of the fluctuation and the influence of grid resolution are examined in more detail based on the longitudinal variation in maximum v_{rms} in Fig. 12. Figure 12 shows that v_{rms} begins to increase within the separated shear layer well upstream of the shock impingement. The growth rate suddenly increases on shock impingement at $x = 58$ mm, and v_{rms} takes a maximum downstream of the reattachment point at $x = 70$ mm. The curve for grid D departs from that for the finer grids at $x = 62$ mm, and the curve for grid C falls below the three finer grids at a similar point ($x = 65$ mm). The curves for grids B and E follow that for the finest grid A up to $x = 67$ mm, where the shear layer reattaches. The influence of the grid resolution is, therefore, most apparent between $x = 67$ and 75 mm. These observations indicate that the grid resolution required to revolve the growth of velocity fluctuation becomes finer downstream. Although the velocity fluctuation during the transition is dependent on the grid resolution, its influence on the mean velocity is limited. As shown in Fig. 8, the velocity profiles for grid B coincide with that for the finest grid A at all five locations.

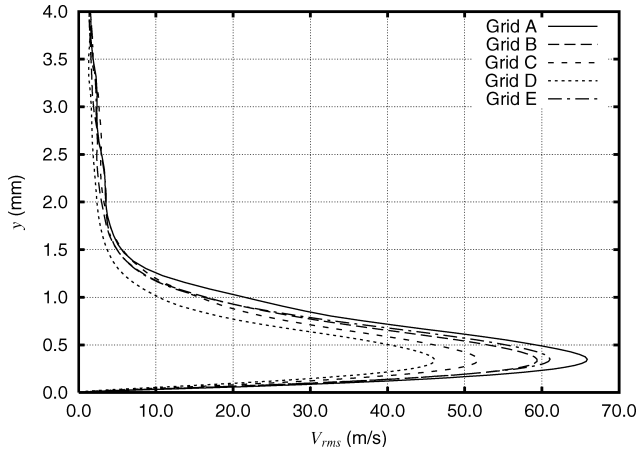

a) $x = 70$ mm

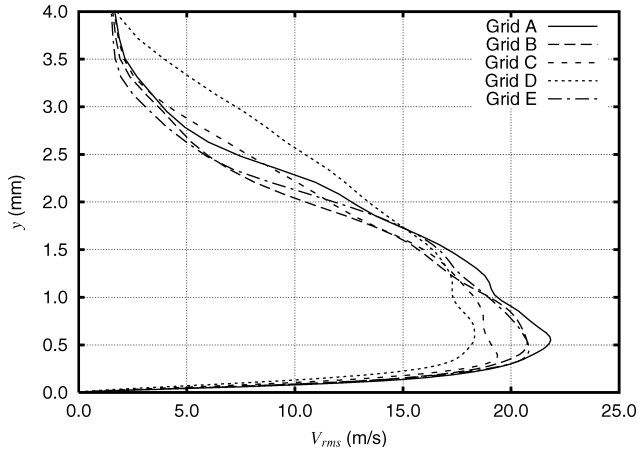

b) $x = 95$ mm

Fig. 11 Wall-normal fluctuation velocity profile.

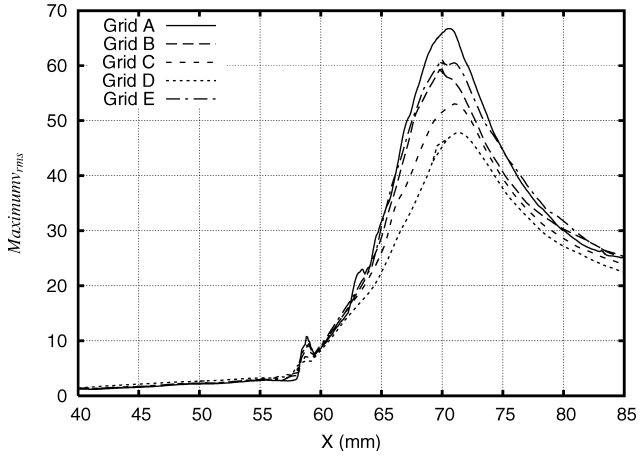

Fig. 12 Longitudinal evolution of maximum wall-normal fluctuation velocity.

The influence of the inlet turbulence level is presented in Fig. 13. These simulations were performed separately from the corresponding two-dimensional laminar solution. The numerical results exhibit a clear dependence on the inlet turbulence, where higher inlet turbulence levels general result in faster growth of the fluctuation inside the shear layer. This leads to earlier reattachment, which shifts the separation point downstream. However, the structure of the flowfield was found to be essentially the same for all four turbulence levels. Because quantitative agreement is not the objective of the present study, the results for $Tu = 0.6\%$, which demonstrated satisfactory agreement with the experimental results, are used in the following discussion. In practical applications, it is often the case that detailed

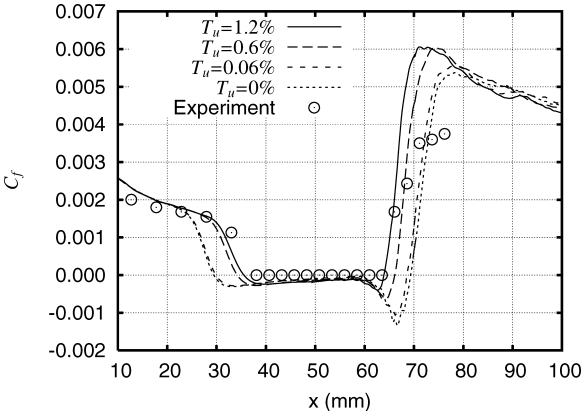

a) Friction coefficient

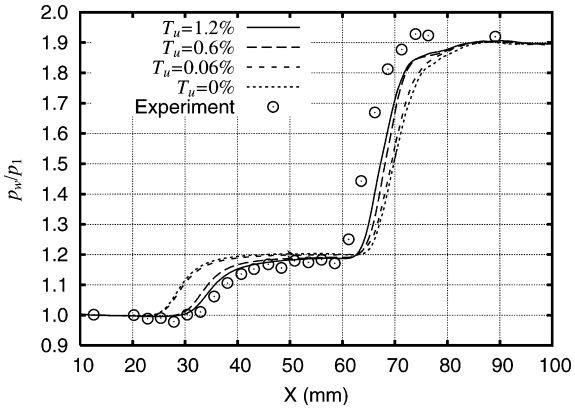

b) Wall pressure distribution

Fig. 13 Influence of inlet turbulence, grid B.

information on the inlet turbulence is not provided. In such cases, a certain degree of tuning is inevitable.

This analysis of the time-averaged flowfield demonstrated that the present LES code provides satisfactory results regarding the reattachment point and the properties of the boundary layer downstream of reattachment, which are the primary concerns in many engineering applications. Through grid refinement it was revealed that the velocity fluctuation in the transitional region is dependent on the grid resolution and that a grid resolution of $\Delta x^+ \sim 40$ and $\Delta z^+ \sim 15$ is required to achieve grid convergence for the reattachment point. This requirement is slightly finer than that that required to resolve a fully turbulent attached boundary layer.

Instantaneous Flowfield

Figure 14 shows snapshots of the instantaneous flowfield at three instants. Figures 14a show the isosurfaces of $u' = -100$ m/s, representing low-speed streaks. Here, u' denotes the streamwise velocity fluctuation, $u'(x, y, z, t) \equiv u(x, y, z, t) - \bar{U}(x, y)$, where $\bar{U}(x, y)$ is the time- and spanwise-averaged streamwise velocity. The shaded areas on the bottom wall in Fig. 14a indicate the region of negative friction coefficient, representing the extent of the separation region. Figure 14b show the isosurfaces of the second invariant of the velocity gradient tensor Q, representing the cores of vortices,[27] as given by

$$Q \equiv \frac{1}{2}\left[\left(\frac{\partial u_k}{\partial x_k}\right)^2 - \frac{\partial u_i}{\partial x_j}\frac{\partial u_j}{\partial x_i}\right]$$

In Fig. 14b, white surfaces denote vortices with $\omega_x > 0$, and dark surfaces denote vortices with $\omega_x < 0$. The lateral vortex near $x \simeq 60$ mm corresponds to the vortex induced by shock impingement, whereas the others vortices occur inside the boundary layer or shear layer.

Figure 14a shows that rows of almost equally spaced low-speed streaks appear at $x \simeq 63$ mm and that the reattachment point is shifted downstream beneath these low-speed streaks. The separation region is intermittent, and although the starting points of the streaks move back and forth, the streaks always begin upstream of

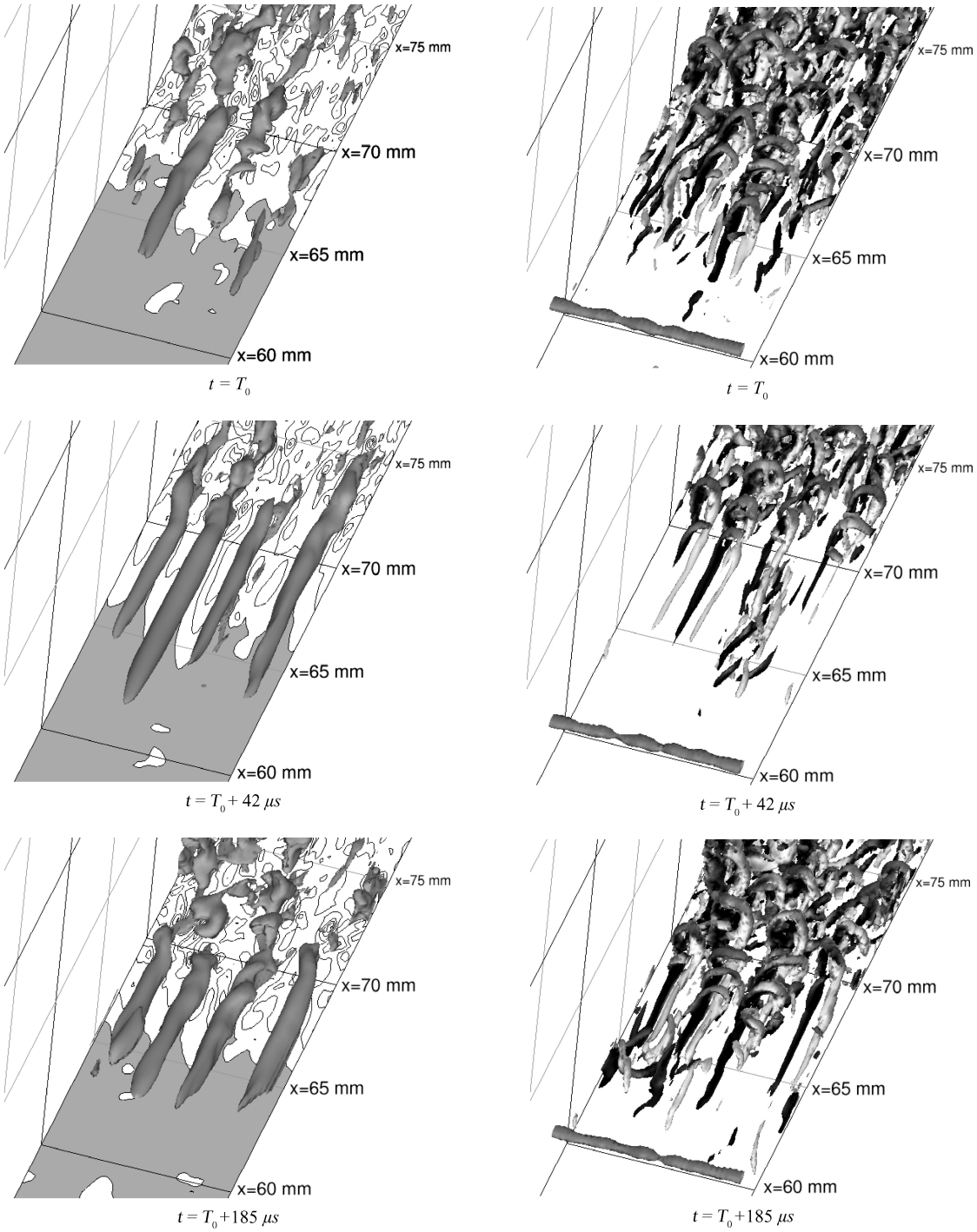

Fig. 14 Instantaneous flowfields, grid B.

the reattachment point. The streaks remain parallel to each other until slightly downstream of the reattachment point, $x \simeq 68$ mm, where they become disturbed. When Figs. 14a and 14b are compared, it becomes clear that a pair of counter-rotating longitudinal vortices is formed alongside each low-speed streak. The neighboring longitudinal vortices are connected, and hairpin vortices (gray) appear near the reattachment point. The formation of these hairpin vortices corresponds to the onset of disturbance of the low-speed streaks. These large-scale coherent structures break down at $x \simeq 73$ mm, and the structure downstream of that point has a much finer length scale and appears more chaotic.

The vortices to the right of the streaks rotate clockwise ($\omega_x > 0$), whereas those to the left rotate counterclockwise ($\omega_x < 0$). Therefore, the pairs of longitudinal vortices induce upward velocity in the region between the vortices. The velocity profiles inside the second leftmost low-speed streak ($z = 1.84$ mm) in Fig. 14a at $t = T_0 + 185\ \mu$s are shown in Figs. 15 and 16. Strong upward velocity of $v \simeq 20$ m/s is induced within the region $0 < y < 0.5$ mm at $x = 65$ mm, immediately upstream of reattachment, and a strong shear layer is formed above that region. This region corresponds to the peak in the Reynolds stress shown in Fig. 4. Figures 15 and 16 indicate that low-speed fluid raised by the upward velocity induced by the pair of longitudinal vortices forms low-speed streaks and an overlying shear layer. Flow instability induced by the steep velocity gradient is considered to be the trigger for the formation of the hairpin vortices.

Note that the formation of low-speed streaks and longitudinal vortex pair corresponds to the location at which $v_{\rm rms}$ for grid D

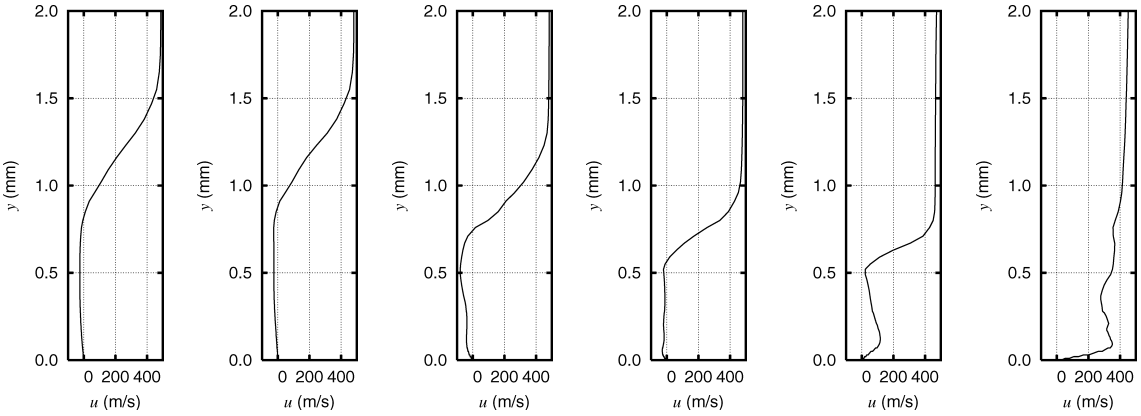

a) $x = 55$ mm **b) $x = 60$ mm** **c) $x = 62$ mm** **d) $x = 65$ mm** **e) $x = 67$ mm** **f) $x = 70$ mm**

Fig. 15 Instantaneous longitudinal velocity inside low-speed streaks in $z = 1.84$ mm plane, grid B.

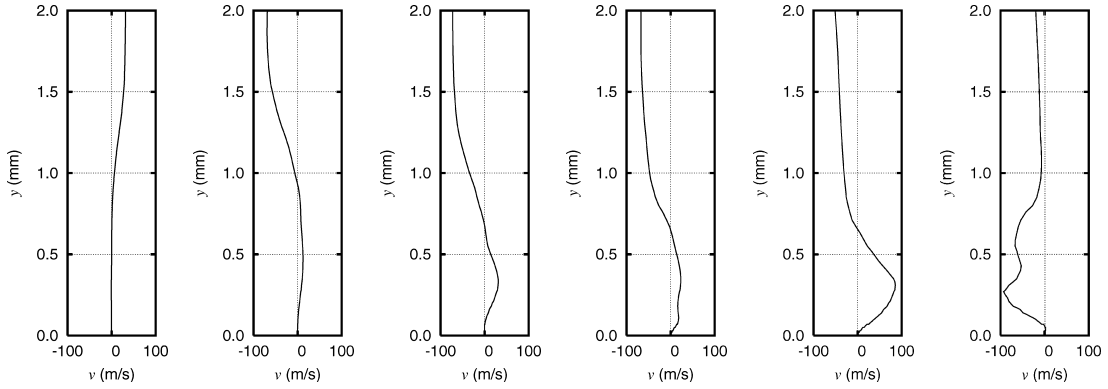

a) $x = 55$ mm **b) $x = 60$ mm** **c) $x = 62$ mm** **d) $x = 65$ mm** **e) $x = 67$ mm** **f) $x = 70$ mm**

Fig. 16 Instantaneous wall-normal velocity inside low-speed streaks in $z = 1.84$ mm plane, grid B.

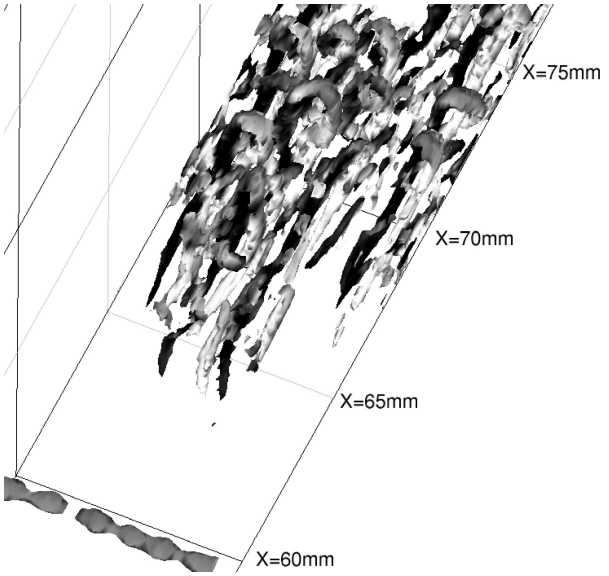

Fig. 17 Q isosurface, grid C.

departs from the values for the finer grids (Fig. 12). The formation of hairpin vortices also corresponds to the point at which v_{rms} for grid C falls below the values for the three finer grids. The breakdown of large-scale coherent structures also corresponds to the region in which the difference between grids A and B is most distinct.

Figure 17 shows the isosurface of Q for grid C. Although the streamwise vortex pairs and hairpin vortices are observable, the structure is somewhat obscure due to the lower spatial resolution. This indicates that underresolution of the large-scale coherent structure is responsible for the underestimation of the fluctuation velocities.

This analysis of the instantaneous flowfield revealed that the longitudinal vortex pairs and hairpin vortices play key roles in determining the behavior of the transition of shock wave/laminar boundary-layer interaction. Therefore, it is important to resolve these structures well to obtain accurate predictions of the reattachment point. The region in which the discrepancy between grids A and B was most distinct, $x = 68$–75 mm, in Fig. 12 corresponds to the region in which these coherent structures break down. The discrepancy indicates that it is necessary to use a much finer grid than grid B to resolve the breakdown adequately. However, Fig. 8e shows that, if the large-scale coherent structure is resolved with sufficient resolution, underresolution of the breakdown process does not influence the boundary-layer profile downstream substantially.

Spanwise Variation of v_{rms}

Figure 18 shows the spanwise variation of wall-normal velocity fluctuation evaluated from the time average over 100 μs. Because the motion of the streaks is very slow (Fig. 14), the streaks can be regarded as a mean component, and the hairpin vortices can be regarded as a fluctuation component with this timescale. The semitransparent surface is the isosurface of a time-averaged Mach number of unity, and the white contours represent the v_{rms} distribution in each section (Fig. 18).

The streak is observable from the Mach number isosurface up to $x = 72.5$ mm. The isosurface downstream of $x = 75$ mm is almost flat, indicating that the large-scale streak structure ends by this point. Peaks in v_{rms} occur at the tops of the streaks at sections $x = 70$ and 72.5 mm. The correlation between v_{rms} peaks and the streaks is not so clear on other sections. The sections $x = 70$ and 72.5 mm correspond to the region in which hairpin vortices are observed at the top of the low-speed streaks (Fig. 14). Thus, these observations

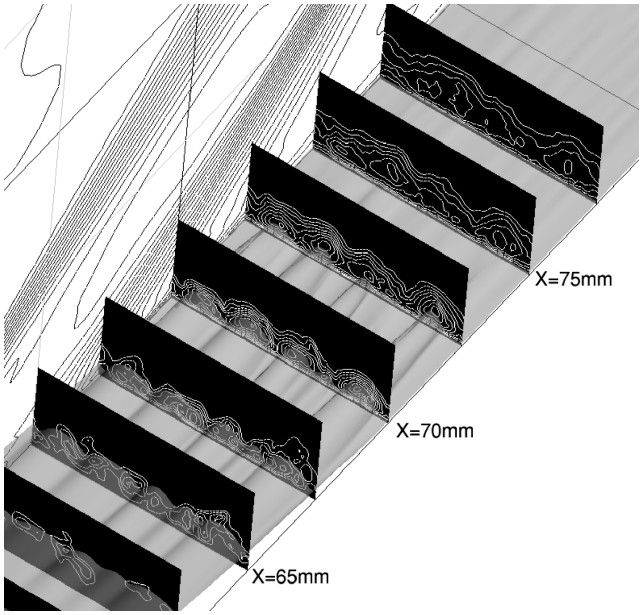

Fig. 18 Spanwise variation of $v_{\rm rms}$ evaluated from time-average over 100 μs, grid B.

also confirm that the $v_{\rm rms}$ peaks in Fig. 12 are correlated with the formation and breakdown of the hairpin vortices.

Conclusions

The transition of a boundary layer on a flat plate with impinging shock waves was studied by compressible LES. The simulation results were found to be comparable with previous experimental results with respect to the reattachment point and the properties of the boundary layer downstream of reattachment, which are the main concerns in many engineering applications. Observations of the unsteady flowfield revealed that large-scale coherent structures such as longitudinal vortex pairs, low-speed streaks, and hairpin vortices play key roles in determining the behavior of the transition of shock wave/laminar boundary-layer interaction. Therefore, it is important to ensure adequate resolution of the coherent structure to obtain accurate predictions of the downstream flowfield. Grid refinement revealed that a grid resolution of $\Delta x \simeq 40^{+}$ and $\Delta z^{+} \simeq 15$, slightly finer than that required for resolving fully turbulent attached boundary layer, is required to resolve the coherent structure.

Resolving the breakdown of the large-scale coherent structure requires much finer spatial resolution, and grid convergence of the fluctuation velocity in the transitional region was not achieved with the grids adopted in this study. If the large-scale coherent structure itself is adequately resolved, underresolution of the breakdown process does not have a excessive impact on the simulated behavior of the downstream boundary layer.

The analysis presented here illustrates how LES can be used for the qualitative analysis of flowfields involving supersonic transitional boundary layers.

Acknowledgments

Some of the numerical simulations presented in this study were performed on the SX/6 supercomputer of Institute of Space and Astronautical Science/Japan Aerospace Exploration Agency as part of joint research with the Center for Planning and Information Systems. Gratitude is extended to Eric Garnier for valuable discussions and the provision of experimental data.

References

[1]Mayle, R. E., "The Role of Laminar–Turbulent Transition in Gas Turbine Engines," *Journal of Turbomachinery*, Vol. 113, No. 4, 1991, pp. 509–537.

[2]Palma, P. D., "Accurate Numerical Simulation of Compressible Transitional Flows in Turbomachinery," *AIAA Journal*, Vol. 40, No. 4, 2002, pp. 702–708.

[3]Michelassi, V., "Shock–Boundary Layer Interaction and Transition Modelling in Turbomachinery Flows," *Proceedings of the Institution of Mechanical Engineers, Part A: Journal of Power and Energy*, Vol. 211, No. 3, 1997, pp. 225–234.

[4]Hilgenfeld, P., Cardamone, P., and Fottner, L., "Boundary Layer Investigations on a Highly Loaded Transonic Compressor Cascade with Shock/Laminar Boundary Layer Interactions," *Proceedings of the Institution of Mechanical Engineers, Part A: Journal of Power and Energy*, Vol. 217, No. 4, 2003, pp. 349–356.

[5]Garnier, E., Sagaut, P., and Deville, M., "Large Eddy Simulation of Shock/Boundary-Layer Interaction," *AIAA Journal*, Vol. 40, No. 10, 2002, pp. 1935–1944.

[6]Rizzetta, D., Visbal, M., and Gaitonde, D., "Large-Eddy Simulation of Supersonic Compression-Ramp Flows by High-Order Method," *AIAA Journal*, Vol. 39, No. 12, 2001, pp. 2283–2291.

[7]Knight, D., Yan, H., Panaras, A. G., and Zheltovodov, A., "Advances in CFD Prediction of Shock Wave Turbulent Boundary Layer Interactions," *Progress in Aerospace Sciences*, Vol. 39, No. 2–3, 2003, pp. 121–184.

[8]Bake, S., Meyer, D. G. W., and Rist, U., "Turbulence Mechanism in Klebanoff Transition: A Quantitative Comparison of Experiment and Direct Numerical Simulation," *Journal of Fluid Mechanics*, Vol. 459, 2002, pp. 217–243.

[9]Berlin, S., Wiegel, M., and Henningson, D. S., "Numerical and Experimental Investigations of Oblique Boundary Layer Transition," *Journal of Fluid Mechanics*, Vol. 393, 1999, pp. 23–57.

[10]Alam, M., and Sandham, N. D., "Direct Numerical Simulation of 'Short' Laminar Separation Bubbles with Turbulent Reattachment," *Journal of Fluid Mechanics*, Vol. 410, 2000, pp. 1–28.

[11]Yang, Z., and Voke, P. R., "Large-Eddy Simulation of Boundary-Layer Separation and Transition at a Change of Surface Curvature," *Journal of Fluid Mechanics*, Vol. 439, 2001, pp. 305–333.

[12]Jacobs, R. G., and Durbin, P. A., "Simulation of Bypass Transition," *Journal of Fluid Mechanics*, Vol. 428, 2001, pp. 185–212.

[13]Wu, X. H., Jacobs, R. G., Hunt, J. C. R., and Durbin, P. A., "Simulation of Boundary Layer Transition Induced by Periodically Passing Wakes," *Journal of Fluid Mechanics*, Vol. 398, 1999, pp. 109–153.

[14]Abdulmalik, A., Lawal, A. A., and Sandham, N. D., "Direct Simulation of Transonic Flow Over a Bump," *Direct and Large-Eddy Simulation IV*, edited by B. J. Geurts, Kluwer Academic, 2001, pp. 301–310.

[15]Vreman, B., "Direct and Large-Eddy Simulation of the Compressible Turbulent Mixing Layer," Ph.D. Dissertation, Dept. of Applied Mathematics, Univ. of Twente, Twente, The Netherlands, June 1995.

[16]Lele, S. K., "Compact Finite Difference Schemes with Spectral-like Resolution," *Journal of Computational Physics*, Vol. 103, No. 1, 1992, pp. 16–42.

[17]Gaitonde, D. V., and Visbal, M. R., "Padé-Type Higher-Order Boundary Filters for the Navier–Stokes Equations," *AIAA Journal*, Vol. 38, No. 11, 2000, pp. 2103–2112.

[18]Ducros, F., Ferrand, V., Nicoud, F., Weber, C., Darracq, D., Gacherieu, C., and Poinsot, T., "Large-Eddy Simulation of the Shock/Turbulence Interaction," *Journal of Computational Physics*, Vol. 152, No. 2, 1999, pp. 517–549.

[19]Lenormand, E., Sagaut, P., and Phuoc, L. T., "Large Eddy Simulation of Subsonic and Supersonic Channel Flow at Moderate Reynolds Number," *International Journal for Numerical Methods in Fluids*, Vol. 32, No. 4, 2000, pp. 369–406.

[20]Ekaterinaris, J. A., "Implicit, High-Resolution, Compact Schemes for Gas Dynamics and Aeroacoustics," *Journal of Computational Physics*, Vol. 156, No. 2, 1999, pp. 272–299.

[21]Thompson, K. W., "Time Dependent Boundary Conditions for Hyperbolic Systems," *Journal of Computational Physics*, Vol. 68, No. 1, 1987, pp. 1–24.

[22]Adams, N., "Direct Numerical Simulation of Turbulent Compression Ramp Flow," *Theoretical and Computational Fluid Dynamics*, Vol. 12, No. 2, 1998, pp. 109–129.

[23]Hakkinen, R. J., Greber, I., Thilling, L., and Abarbanel, S. S., "The Interaction of an Oblique Shock Wave with a Laminar Boundary Layer," NASA Memo 2-18-59W, March 1959.

[24]Dimas, A., Mowli, B., and Piomelli, U., "Large-Eddy Simulation of Subcritical Transition in an Attachment-Line Boundary Layer," *Journal of Fluid Mechanics*, Vol. 387, May 1999, pp. 353–396.

[25]van Driest, E. R., "Turbulent Boundary Layer in Compressible Fluids," *Journal of the Aeronautial Sciences*, Vol. 18, No. 3, 1951, pp. 145–160.

[26]Spalart, P. R., "Direct Simulation of a Turbulent Boundary Layer up to $R_theta = 1450$," *Journal of Fluid Mechanics*, Vol. 187, 1988, pp. 61–98.

[27]Zhou, J., Adrian, R. J., Balachandar, S., and Kendall, T. M., "Mechanism for Generating Coherent Packets of Hairpin Vortices in Channel Flow," *Journal of Fluid Mechanics*, Vol. 387, 1999, pp. 353–396.

D. Gaitonde
Associate Editor